A WORKFLOW TO ESTIMATE RESERVOIR PROPERTIES OF UNCONVENTIONAL GAS SHALES: A CASE STUDY OF THE HAYNESVILLE SHALE

Meijuan Jiang

Department of Geological Sciences
The University of Texas at Austin

ABSTRACT

Reservoir properties, such as porosity, composition, and pore shape of gas shales are important for both exploration and production purposes of these complex reservoir rocks. This work presents a workflow to invert these properties from well log sonic data for unconventional gas shales, using the Haynesville Shale as a case study. Two rock physics models, an isotropic and an anisotropic one, were combined with a grid search method. The isotropic model initiates the numerical simulation by including grains and pores of different shapes and sizes; the anisotropic model then treats the shale as a vertical transversely isotropic medium by introducing aligned fractures. After the relationships between the reservoir properties and elastic properties (P- and S- wave velocities) were built through the rock physics models, a grid search method was used to estimate the reservoir properties and the associated uncertainties. In the grid searching, P- and S-wave velocities from the rock physics models were compared with the measured log data. The modeled seismic velocities that satisfied specific acceptance criteria provided the estimated reservoir properties. The workflow was applied to the Haynesville Shale and provided joint distributions of porosity, composition and pore aspect ratio at the well location. The porosity and composition estimations matched the observations from log and core data within a few percent. Aspect ratio estimation matched those observed in microscale images. When we apply this workflow to the seismic scale where there are continuous seismic velocities inverted from 3D seismic data, we will be able to obtain spatial distributions of these reservoir properties and, therefore, provide optimal locations for exploration and production wells.

INTRODUCTION

Estimation of reservoir properties, such as porosity, composition, and pore shape of gas shales and other unconventional hydrocarbon systems are important for both exploration and production. Understanding these reservoir properties contributes to identifying zones of economic production and possibly optimal zones for hydraulic fracturing. Porosity estimation helps to determine gas capacity and the estimated ultimate recovery (EUR); composition

contributes to understand shale brittleness, and pore aspect ratio provides additional information to determine the stiffness of the shale.

To understand reservoir properties of shales, rock physics models are very important. Rock physics models describe the relationships between reservoir properties and the elastic properties, calibrated by well log data and core data at well locations. The specific rock physics model to be used depends on the rock type and complexity of the rock. The complexity we consider important for gas shales are the relationships among lithology, porosity, fluid, pore shape, pressure and anisotropy. Although numerous contact-theory models (Dvorkin and Nur, 1996; Gal et al., 1998; Avseth et al., 2000), empirical rock-physics relationships (Tosaya and Nur, 1982; Castagna et al., 1985) and inclusion-based models (Kuster and Toksoz, 1974; O'Connell and Budiansky, 1974) exist, few of them are capable of modeling complex shales in terms of pore and grain shapes, composition, and anisotropy. The Haynesville Shale tends to have flattened or elongated grains and pores (Curtis et al., 2010). These flattened or elongated grains and pores significantly reduce the velocities of the shale, because the shape is compliant, which reduces the rock moduli, depending on the orientation of pores relative to wave propagation and/or polarization directions. In addition, shales are typically anisotropic due to either intrinsic alignment of clay platelets or alignment of pores, cracks or fractures. Therefore, to model and understand gas shales, we must utilize more complicated models.

Unlike conventional clastic reservoirs, for which there are numerous studies estimating distributions of porosity, clay content, water saturation, lithology facies and fluid types from seismic data (e.g., Mukerji et al., 2001; Eidsvik et al., 2004; Bachrach, 2006; Spikes et al., 2007; Grana and Della Rossa, 2010; Rimstad et al., 2012), characterizing reservoir properties of gas shales is still a young and very active area of research. Vanorio et al. (2008) used vitrinite reflectance data to generate relationships between maturity and Thomsen's (1986) anisotropic parameter ε to understand how maturation processes cause anisotropy changes. Delle Piane et al. (2011) investigated the intrinsic and crack-induced anisotropy of brine-saturated shale samples under different external stresses. They found that elastic anisotropy of these samples depended on the composition and spatial distributions of different minerals and microfractures, and the change of anisotropy depended on the applied stresses, their orientations and the degree of stress anisotropy. Nadri et al. (2012) presented an approach to estimate the anisotropy parameters of transversely isotropic shales of arbitrary geometry. They successfully applied this approach on ultrasonic P-wave velocity data from a spherical shale sample and a cylindrical shale sample. Those studies were based on laboratory measurements of shale samples. There were also studies modeling elastic properties of shales. Dræge et al. (2006) combined the self-consistent model and a differential effective medium model with a shale compaction theory to model the effective elastic stiffness of shales as a function of depth, as well as estimating the effect of cementation

on the effective elastic stiffness of shales. Their modeled results were consistent with the vertical P- and S-wave velocities from three wells. Avseth et al. (2008) used rock physics and AVO depth trend modeling to understand the physical properties (intrinsic anisotropy, smectite-to-illite transition, AVO attributes) of mechanically compacted shales as function of burial depth, and therefore improved characterization on sandstone reservoirs embedded in shales. Ciz and Shapiro (2009) were able to explain the compliance tensor, anellipticity, and three anisotropic parameters under different stresses for transversely isotropic shales through a porosity-deformation approach and its anisotropic extension. Pervukhina et al. (2011) described the five stress-dependent elastic coefficients of transversely isotropic shales using a model that treated the orientation of clay platelets and compliance ratio of the platelet contacts as inputs. Their model was able to predict simultaneously the stress dependency of all five elastic compliances. Recently, Jiang and Spikes (2012) used the self-consistent model and a grid search method to estimate porosity and pore shape distributions for the Haynesville Shale. In that study, only P-impedance was included to estimate either porosity or pore shape under isotropic condition, and anisotropy was not considered.

This study provides a comprehensive understanding of the porosity, composition, and pore shape distributions of the Haynesville Shale constrained by both P- and S-wave velocities through a combination of rock physics models and grid searching. The rock physics models used here combined an isotropic effective medium model (the self-consistent model, O'Connell and Budiansky, 1974; Berryman, 1980) and an anisotropic effective medium model (Chapman, 2003). The self-consistent model provided a porous rock matrix with multiple mineral phases and pores with different aspect ratios. The anisotropic effective medium model based on Chapman (2003) provided frequency- and pore-pressure-dependent anisotropy. Relationships between reservoir properties and elastic properties were obtained by correlating input rock property distributions and combining these two models. Based on these relationships, the grid search provided distributions of porosity, composition, and pore shapes by considering all the possible modeled solutions without bias.

STUDY AREA AND DATA

The Haynesville Shale, located at the boundary of Texas and Louisiana, is in the Sabine Uplift and west of the North Louisiana Salt Basin. The depositional environment is interpreted as a deep and partly euxinic and anoxic restricted basin that was surrounded by carbonate platforms and siliciclastic shelves during the upper Jurassic (Hammes et al., 2011). It lies stratigraphically above the Smackover limestone formation and beneath the Cotton Valley Group. Reservoir depth varies from 3000–4700 m. The major mineralogic components are clay, quartz and calcite,

and the gas capacity is estimated at more than 100 tcf (Hammes et al., 2011). The permeability is extremely low (less than 0.001 mD on average), and the porosity varies from about 3% to 14% (Wang and Hammes, 2010). The Haynesville Shale has been shown to exhibit vertical transverse isotropy (VTI) (Horne et al., 2012).

Data from two vertical wells, one inside and one outside a seismic survey area, were used in this study. These two wells (Well A and Well B) are approximately 3 km away from each other. Well A is inside the seismic survey area, but Well B is out of the survey area. Gamma ray, caliper, density, P- and S-wave velocity (V_P and V_S), and P-impedance are plotted (Well A in Figure 1 and Well B in Figure 2). The Haynesville Shale (gray shaded zone) was identified based on the increase of gamma ray log (Well A) and decrease of the density log (Well B). Above the Haynesville Shale is the Bossier Shale, and the Smackover Limestone is below the Haynesville Shale. Overall, V_P and V_S in each well are very well correlated, and they are inversely correlated with the gamma ray log. The logs from these two wells show very similar features except that Well B has better data quality than Well A whose borehole environment is rugose as indicated by the caliper log. The density, V_P and V_S logs in Well A have many fluctuations that diminish their reliability. Therefore, we focused on the log data from Well B when inverting reservoir properties from elastic properties. In Well B, within the Haynesville Shale formation, density varies from 2.43 to 2.67 g/cm^3 with an average of 2.53 g/cm^3. The V_P varies from 2.93 to 4.07 km/s, with an average of 3.26 g/cm^3; the V_S varies from 1.68 to 2.47 km/s, with an average of 1.94 km/s.

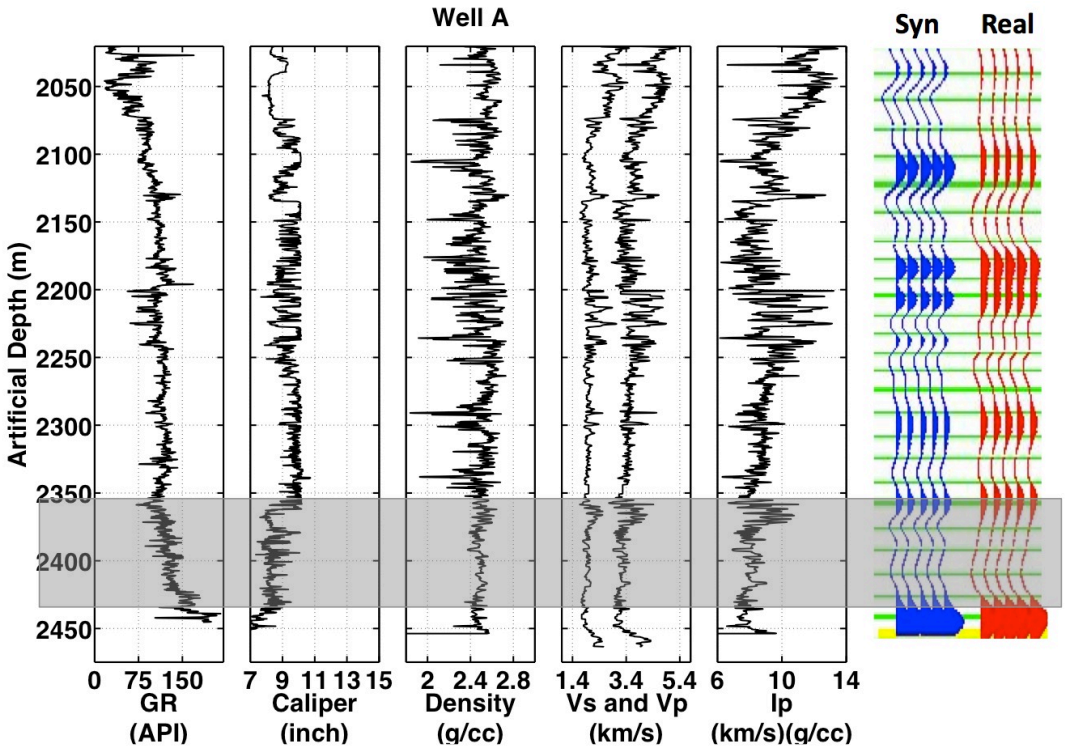

Figure 1. Well log data and seismic data from Well A. Gamma ray, caliper, density, P- and S-wave velocities (V_P and V_S), and P-impedance are plotted. Depth is artificial. The Haynesville Shale is marked as the gray shaded zone. It is identified based on the increase of gamma ray log. On the right seismic data at Well A is plotted. Overall, VP and VS are very well correlated, and they are inversely correlated with the gamma ray log. The caliper log has many fluctuations, indicating a rugose borehole environment that causes fluctuations in the density and velocity logs. The blue seismograms are five duplicates of the synthetic seismic data, and red seismograms are five duplicates of the observed seismic data at the well location. Seismic data were tied to the well log data with a correlation coefficient of 0.79. The seismic data indicate large reflectivity at the bottom of the Haynesville Shale, whereas the top of Haynesville Shale is not as clearly identifiable as the bottom.

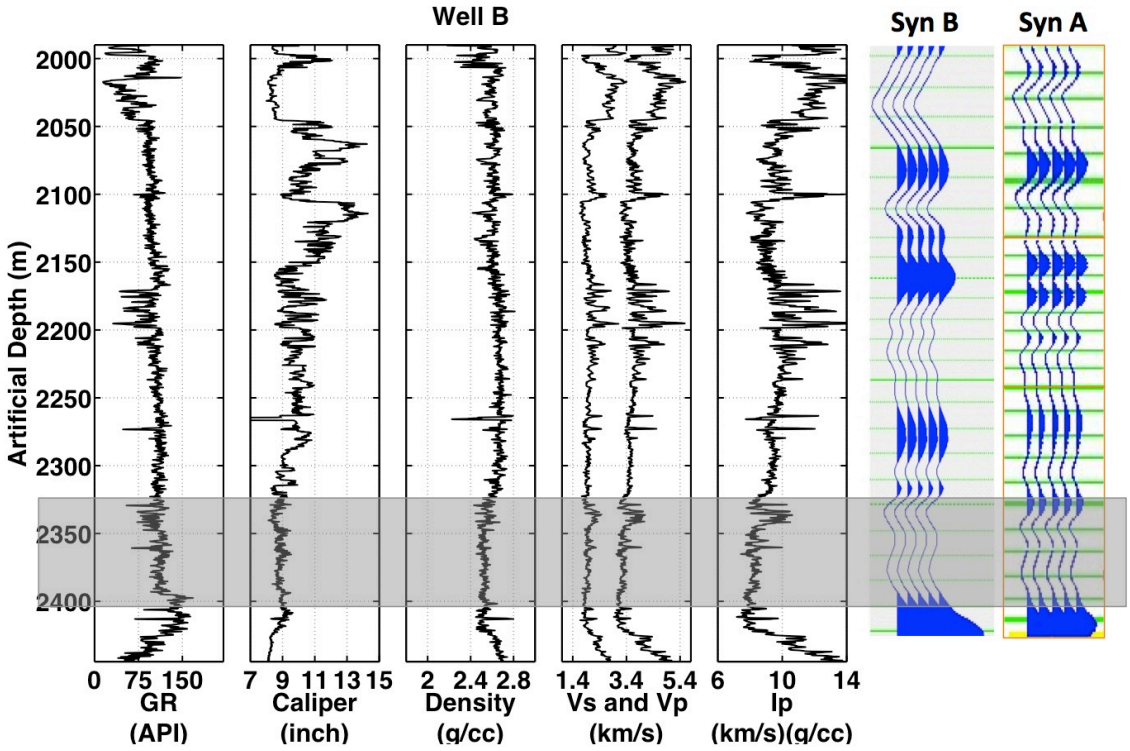

Figure 2. Well log data from Well B. Gamma ray, caliper, density, P- and S-wave velocities (V_P and V_S), and P-impedance are plotted. Depth is artificial. The Haynesville Shale is marked as the gray shaded zone, identified by the decrease of density due to high kerogen content. Well B has better data quality than Well A. Overall, V_P and V_S are very well correlated, and they are inversely correlated with the gamma ray log. On the right, synthetic seismic data from Well B is plotted, generated by the same wavelet from Well A. Both have five duplicates. Because these two wells are close to each other (less than 3 km), their synthetic seismograms are similar.

For both wells, synthetic seismograms generated from the impedance logs are plotted with the log data. In Well A (Figure 1), the observed seismic data (red seismograms) were tied with the log data by using time-to-depth information generated by VSP travel times from an adjacent well, which was not included in this work. The observed seismic data and synthetic seismic data are very similar with a correlation coefficient of 0.79. Because there is no observed seismic data for Well B, its synthetic seismograms were compared with the synthetic ones from Well A. The same wavelet (extracted from observed seismic data at Well A) were used for both Well A and Well B. Because the impedance log of Well A fluctuates due to the rugose borehole environment, the synthetic seismogram for Well A appears to have higher frequency than the one from Well B. The seismic data indicates large reflectivity difference between the Haynesville Shale and the underlying Smackover Limestone due to the large increase of V_P and density. However, the boundary between the Hayesville Shale and Bossier Shale is not as clearly defined as the one between the Haynesville Shale and Smackover Limestone.

In addition to log and seismic data, core data were available for Well A. Forty-eight samples within the Bossier and Haynesville Shale formations were measured at about a 3-m interval.

Among these 48 samples, 20 were for Bossier and 28 were for Haynesville Shale. X-Ray diffraction (XRD) and density analysis provided composition information. Both the Bossier and Haynesville Shale contain quartz, feldspar, plagioclase, calcite, dolomite, pyrite, kerogen and clay (Figure 3). There is a clear boundary between the Bossier and Haynesville Shale due to the composition change. From the Bossier to the Haynesville, the average quartz percentage increases from 28.9% to 31.7%, average calcite percentage increases from 4.8% to 14.2%, average kerogen percentage increases from 1.2% to 5.2%, and average clay percentage decreases from 56.1% to 35.6%. In general, the Haynesville Shale is richer in organic matter but contains less clay than the Bossier Shale.

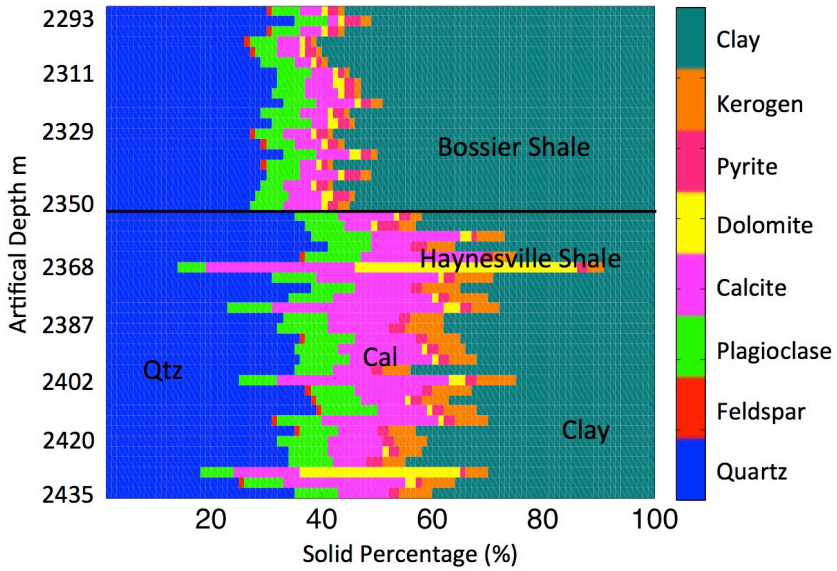

Figure 3. Mineralogic composition of the Bossier and Haynesville Shale from XRD and density analysis for Well A. The depth scale is not linear because the 48 samples were not measured at exactly equal spacing along depth. There is a clear boundary between Bossier and Haynesville Shale due to the increase of quartz, calcite and kerogen and the decrease of clay.

Because XRD and density analysis was done at every 3 m, whereas log data was measured at a 0.15-m interval, we interpolated the 28 samples within the Haynesville Shale formation and then calculated the density porosity as a function of depth based on density log (Equation 1). In Equation 1, ϕ is porosity, ρ_m is the density of the rock matrix, derived from interpolated XRD results, ρ_b is the measured density, and ρ_{fl} is density of the pore fluid.

$$\phi = \frac{\rho_m - \rho_b}{\rho_m - \rho_{fl}} \tag{1}$$

To simplify the modeling to an extent, we included only quartz, calcite, pyrite, kerogen and clay in the rock physics models. We transferred the percentages of feldspar, plagioclase and dolomite from the XRD and density analysis to calcite. Then the average percentages of quartz, calcite, pyrite, kerogen, and clay are 31.59%, 25.79%, 1.96%, 5.28%, and 35.38% for Well A, respectively. Fluid density was calculated from a brine and gas mixture with an average water saturation of approximately 25% based on the resistivity log.

METHOD

A combination of rock physics modeling and grid searching was applied to simultaneously estimate the distributions of porosity, composition and pore shape for the Haynesville Shale. Rock physics modeling provided relationships between the reservoir properties and elastic properties, calibrated to P- and S-wave measurements. The grid searching provided probabilistic estimates of reservoir properties conditioned by the relationships between reservoir properties and elastic properties.

The Haynesville Shale is vertically transversely isotropic (VTI) (Horne et al., 2012), although the degree of anisotropy at the well log scale is not known exactly. Elastic properties of VTI media have a vertical axis of symmetry, generalized as a stack of horizontal layers. Five independent stiffness tensor components in the Voigt notation define VTI media (Thomsen, 1986): C_{11}, C_{33}, C_{44}, C_{66}, and C_{13}. Velocities propagating along and perpendicular to the axis of symmetry, and at angles in between, depend on these five components and the bulk density. We used Chapman's (2003) model to calculate the five components based on the rock matrix built from the self-consistent model. Chapman's model is an effective medium model that imposes anisotropy from aligned fractures. Compared to other transversely isotropic models (Hornby et al., 1994; Dræge et al., 2006; Ciz and Shapiro, 2009; Kuila et al., 2011; Pervukhina et al., 2011; Nadri et al., 2012), Chapman's model considers frequency and pore pressure effects.

Chapman's model (Chapman, 2001; Chapman et al., 2002; Chapman, 2003) was introduced to account for squirt flow in the computation of effective moduli of either isotropic or anisotropic rocks. Squirt flow is the fluid interaction caused by the pressure gradient at micro-scale during wave propagation when the wavelength is smaller than the pore size (Dvorkin and Nur, 1993; Dvorkin et al., 1994). The localized fluid flow usually follows directions different from the direction of wave propagation. In Chapman's model, the rock contains spherical pores, randomly aligned non-spherical cracks, and aligned fractures. The modeled anisotropy results from the aligned fractures. The sizes of spherical pores, non-spherical cracks, and fractures affect the characteristic frequency of the squirt flow, attenuation and velocity dispersion. Non-spherical cracks and fractures both have idealized ellipsoidal shapes, and their aspect ratios are defined as

the ratios between the smallest axis and largest axis. The five stiffness components are calculated from Equation A1–A5. The velocities perpendicular to the fractures were calculated from Equation 2 (Thomsen, 1986).

$$V_P = \sqrt{\frac{C_{33}}{\rho}}$$
$$V_S = \sqrt{\frac{C_{44}}{\rho}} \tag{2}$$

As an extension of his earlier work (Chapman, 2003), Chapman (2009) developed a technique to include two fracture sets with different scale lengths and orientations. Because the Haynesville Shale was treated as a VTI medium with only one axis of symmetry, we implemented the model from Chapman (2003) in this study. Some limitations apply when using this model on the Haynesville Shale. For example, the model assumes that the anisotropy only comes from aligned fractures, whereas aligned clay minerals likely contribute to the VTI anisotropy. Also, Chapman's model contains only one solid phase, and it assumes the pores are spherical, whereas the Haynesville Shale contains multiple minerals phases; and its pores are primarily non-spherical based on microstructure images (Curtis et al., 2010).

To solve these issues, we combined Chapman's model with an additional rock physics model to a build porous rock matrix that included multiple mineral phases and non-spherical pores. The additional model was the self-consistent model (O'Connell and Budiansky, 1974; Berryman, 1980), which is not limited to specific compositions, and is able to incorporate multiple mineralogical and pore phases, as well as their shapes and spatial distributions. The self-consistent model provides the effective moduli for the porous rock matrix consisting of quartz, calcite, pyrite, kerogen, clay and non-spherical pores. The general form of the self-consistent approximation is shown in Equation 3 (Mavko et al., 2009). This pair of equations must be solved iteratively in order to find the yet-to-be determined values of K_{SC} and μ_{SC} as a function of the volumetric quantities and elastic moduli of the constituents.

$$\sum_{i=1}^{N} f_i(K_i - K_{sc})U_i = 0$$
$$\sum_{i=1}^{N} f_i(\mu_i - \mu_{sc})V_i = 0 \tag{3}$$

In these equations, f_i is the fraction of each phase in the rock, K_i and μ_i are the bulk and shear moduli of each phase, K_{SC} and μ_{SC} are the effective moduli to be determined, and U_i and V_i are geometric factors based on moduli of each phase and their aspect ratios.

The combination of Chapman's model and the self-consistent model (Figure 4) provided relationships between elastic and reservoir properties for the Haynesville Shale. After that, a grid search method (Sen and Stoffa, 1995) was used to invert the reservoir properties from the elastic properties. The solutions of the reservoir properties were obtained by systematically searching through each point in the model space composed of elastic properties. Specifically, the model space contained a large number of points on a uniform grid. At each point, the objective functions (Equation 4) were evaluated. In the equation, V_{Pmodel} and V_{Smodel} are the P- and S-wave velocities from the rock physics modeling, and $V_{Pobserved}$ and $V_{Sobserved}$ are the observed P- and S-wave velocities. The velocity values that provided the minima of the objective functions corresponded to the best solutions of the reservoir properties. In this work, we obtained the best solutions and probability distributions at each depth point. The advantage of the grid search method is that the range of values for the model space can be specified, and all the possible solutions are equally considered without any bias. The disadvantage of the grid search method is that it can be time consuming and computationally expensive, depending on the number of points in the model space. The computational cost increases exponentially each time one more property is added (LaValle et al., 2004). In addition, the range of values for the model space should be carefully selected in order to include all physically reasonable possibilities.

$$\begin{aligned} Obj\_P &= |V_{P\text{model}} - V_{P\text{observed}}| \\ Obj\_S &= |V_{S\text{model}} - V_{S\text{observed}}| \end{aligned} \tag{4}$$

In this study, V_P and V_S form the model space, and they are used to estimate jointly three reservoir properties (pore aspect ratio, porosity, and composition). There are two knowns but three unknowns, so the problem is underdetermined. Therefore, correlations among the prior distributions of these three reservoir properties were introduced when generating V_P and V_S from the rock physics models. Those correlations are described in the next section.

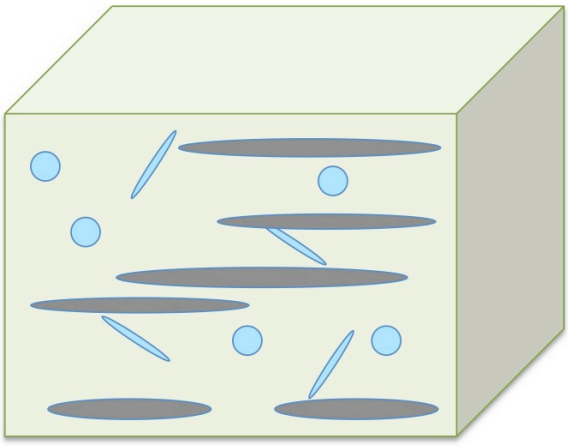

Figure 4. The model assumes a mineral matrix generated by the self-consistent model that contains multiple mineral phases and non-spherical pores with different aspect ratios. In the model, there are distributions of pore shapes from the self-consistent model, and randomly distributed round pores, randomly distributed and oriented microcracks, and aligned fractures from Chapman's model. Cracks and fractures have the same aspect ratio as the non-spherical pores in the self-consistent model, and cracks and fractures have a defined density. Anisotropy comes from the aligned fractures in Chapman's model. Squirt flow was considered in the computation of the five stiffness tensor components for the anisotropic medium in Chapman's model.

WORKFLOW

The combination of the self-consistent model and Chapman's model provided elastic properties (V_P and V_S) given the prior distributions of the reservoir properties (composition, porosity, and pore shape). The prior distributions of these reservoir properties were assumed to contain all possible cases within the defined range. Each combination of reservoir properties corresponded to one set of modeled V_P and V_S. Grid searching inverted the combination of reservoir properties by comparing model V_P and V_S to the observed V_P and V_S.

In the workflow, we first assumed the prior composition distribution that contained 400 mineral assemblages with different percentages of quartz, calcite, pyrite, kerogen, and clay (Figure 5a). This number (400) is enough to maintain high accuracy but low computational cost. In each case, percentages of quartz, calcite, kerogen and clay were varied. Pyrite was fixed as 2%. From the composition assemblages 1 to 400, percentages for quartz and calcite decreased, and percentages for kerogen and clay increased, so the stiffness of the rock matrix decreased as the case number increases. Because the self-consistent model requires aspect ratios for both mineral and pore phases, we assumed the aspect ratios were 1 for stiff quartz, calcite and pyrite, 0.1 for soft clay, and 0.01 for soft kerogen.

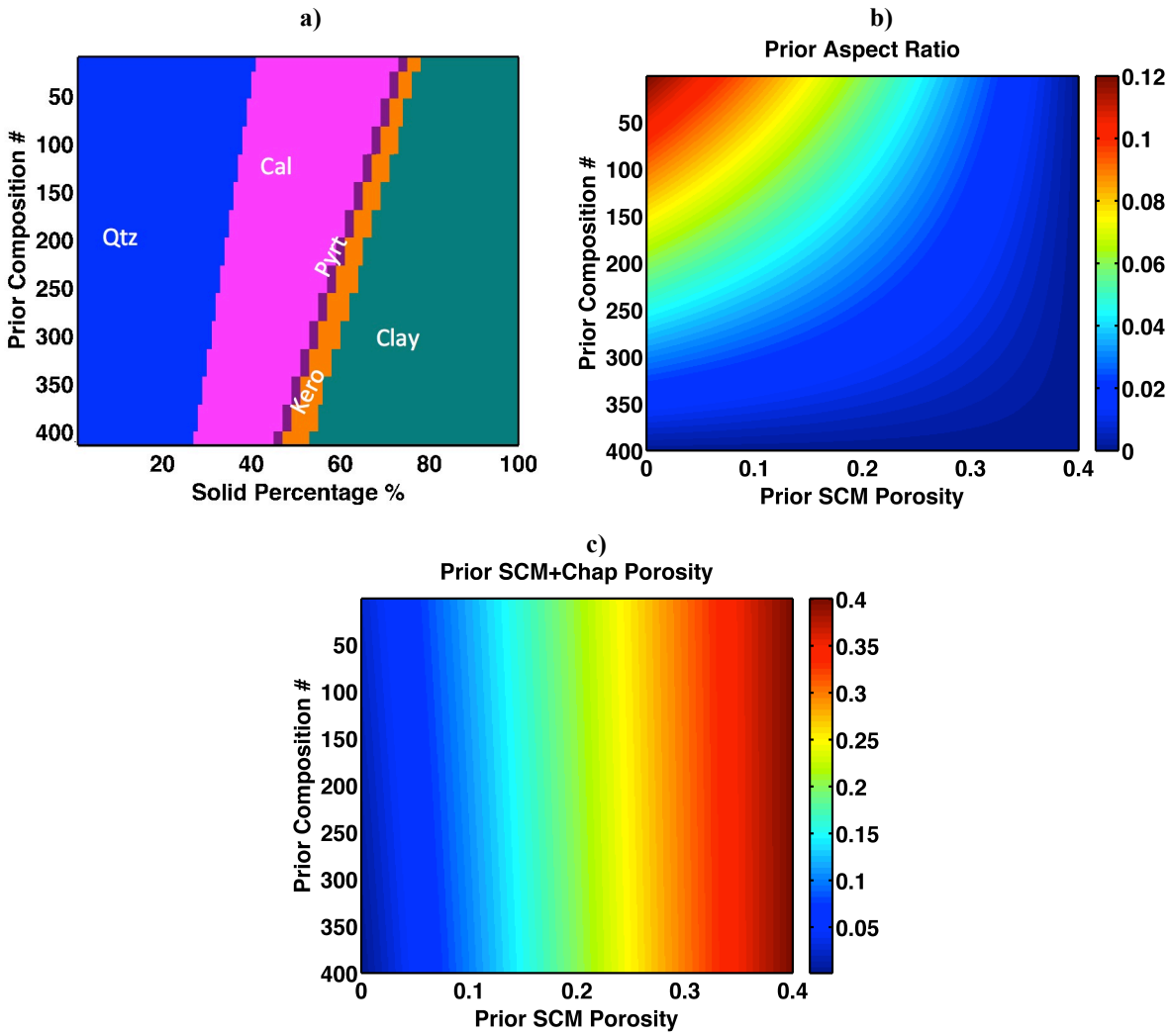

Figure 5. a) The 400 prior composition assemblages used in the modeling. In each case, percentages of quartz, calcite, kerogen and clay were changed. The percentage of pyrite was fixed as 2%. b) The prior aspect ratio distribution based on both prior composition and porosity distribution. To solve three unknowns based on two knowns, the prior aspect ratio was correlated with the prior composition and prior SCM porosity. The aspect ratio was positively linearly related to rock matrix stiffness and negatively linearly related to SCM porosity. The aspect ratio decreases from 0.12 for the smallest SCM porosity and stiffest rock matrix to nearly 0 for the largest SCM porosity and the softest rock matrix. c) The total prior porosity distribution. It contains porosity for SCM and Chapman's model. The porosity from Chapman's model varies with aspect ratio. Therefore, the prior total porosity distribution is not a simple uniform distribution between 0 and 0.4.

The total porosity in the workflow was defined as a function of four different porosity types. Those four included the non-spherical pore porosity in self-consistent model (SCM porosity) and spherical pores, cracks, and fractures in the Chapman's model. The SCM porosity is introduced first. Prior SCM porosity was uniformly distributed between 0 and 0.4, with an increment of 0.01. This large porosity range assures that all the likely porosity values were included in the

model. Because there are three properties to be inverted from two known variables (V_P and V_S), we linearly correlated the prior aspect ratio with the prior composition and prior SCM porosity (Figure 5b). The aspect ratio was positively related to the rock matrix stiffness and negatively related to the SCM porosity. As the clay percentage increased, the pore aspect ratio decreased; as SCM porosity increased, the pore aspect ratio decreased. The aspect ratio decreases from 0.12 for the stiffest rock matrix with smallest SCM porosity to nearly 0 for softest rock matrix with largest SCM porosity. Based on the prior distributions of composition, SCM porosity and pore aspect ratio, a porous rock matrix was generated from the self-consistent model.

In Chapman's model, we assumed that the frequency was 10 kHz, near the frequency of the log data. Because pores in Haynesville Shale are unlikely to be spherical, the contribution from round pores ϕ_{rp} was set to be 0.1%. Crack density ε_c was assumed to be 0.01, and fracture density ε_f was assumed as 0.04. Correspondingly, crack and fracture porosities (Equation 5) were calculated from crack and fracture densities. The total porosity depended on the porosities from both the self-consistent model and Chapman's model. It (ϕ_{total}) was calculated from the solid fraction in the self-consistent model ($1-\phi_{scm}$) and solid fraction in Chapman's model ($1-\phi_{chap}$) using Equation 6. This total porosity was correlated with the prior composition and the prior SCM porosity (Figure 5c). In the model, squirt flow was considered from the porosities in Chapman's model, and the SCM porosities do not contribute to squirt flow.

$$\begin{aligned} \phi_c &= \frac{4\pi\alpha}{3}\varepsilon_c \\ \phi_f &= \frac{4\pi\alpha}{3}\varepsilon_f \end{aligned} \tag{5}$$

$$\begin{aligned} \phi_{total} &= 1-(1-\phi_{scm})\times(1-\phi_{chap}) \\ \phi_{chap} &= \phi_{rp}+\phi_c+\phi_f \end{aligned} \tag{6}$$

From the combination of the self-consistent model and Chapman's model, we obtained modeled V_P and V_S values for each set of composition, porosity, and aspect ratio. The modeled V_P and V_S were compared with observed V_P and V_S from the log data (Equation 4). If the differences between the modeled and observed V_P and V_S were less than 0.08 km/s (~2% error for V_P and ~4% error for V_S), then the corresponding set of reservoir properties (pore aspect ratio, porosity, and composition) were accepted. In this work, we not only obtained the best solutions, but also probability distributions of multiple solutions. The procedure was repeated at each depth in the log data to obtain independent distributions of porosity, composition and pore aspect ratio.

ELASTIC PROPERTIES OF CLAY, KEROGEN AND FLUID

The shale model we built contained quartz, calcite, pyrite, kerogen, clay, and pores/cracks/fractures with brine and gas saturation. Elastic properties for quartz, calcite and pyrite are very well known, and they have small uncertainties. However, the properties for clay, fluid, and kerogen are ambiguous and have large uncertainties. We investigated how different clay and fluid property values affected the modeling results.

It is difficult to measure the elastic properties of clay because clay mineral grains are very small, and they tend to have chemical reactions with organic polar molecules (Theng, 1974; Wang et al., 2001; Vanorio et al., 2003; Moyano et al., 2012). Different types of clay, such as smectite, chlorite and kaolinite, have different bulk and shear moduli and densities due to different mineralogy, structure, and ability to hold clay-bound water. For example, smectite absorbs much more water in volume than illite (Whitney, 1990; Saffer and Marone, 2003), and it has much lower bulk and shear modulus than illite and other clays as a result (Wang et al., 2001). From extrapolation of empirical dependences to pure clay, Castagna et al. (1985), Tosaya and Nur (1982) and Han et al. (1986) obtained similar elastic properties with each other. Wang et al. (2001) obtained much higher bulk and shear moduli through measurements on clay epoxy artificial samples. Vanorio et al. (2003) obtained very low bulk and shear moduli of clay as functions of pressure and saturation through independent experimental methods. By using a generalized singular approximation method of effective media theory, Bayuk et al. (2007) were able to invert a stiffness tensor of clay and obtain its anisotropy parameters. Overall, the elastic properties of various clay minerals have large uncertainties, with the bulk modulus variations from less than 10 GPa to greater than 60 GPa.

To investigate the effects of varying clay properties on the modeling, we tested the bulk modulus of clay from 10 GPa to 60 GPa. The shear modulus of clay was set as 0.47 times the bulk modulus based on Wang et al. (2001). Clay density varied from 2.4 g/cm^3 to 2.7 g/cm^3, and porosity was assumed to be 5%, which is about the average value in the Haynesville Shale. The effective V_P, V_S and V_P/V_S ratio from the combined self-consistent model and Chapman's model are shown in Figure 6. From the softest clay to stiffest clay, both V_P and V_S increase about 30%, and V_P/V_S ratio decreases about 2.2%. This suggests that the effect of clay on velocities is not negligible. Because clay minerals typically absorb water, which makes in situ clay composites softer than pure clay minerals (Wang et al., 2001; Vanorio et al., 2003), we used the relatively soft clay properties from classic gulf type clays (Tosaya, 1982; Han et al., 1986; Blangy, 1992), with bulk modulus of 21 GPa, shear modulus of 7 GPa, and density as 2.58 g/cm^3 (Table 1).

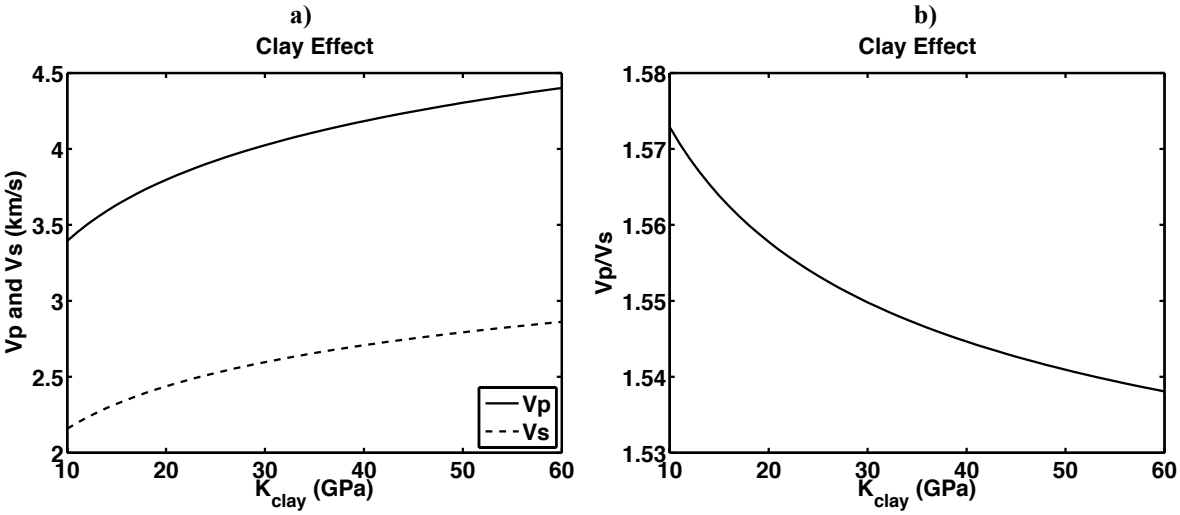

Figure 6. Investigation of how V_P, V_S, and V_P/V_S vary with different clay elastic moduli and densities, due to large uncertainties on elastic properties of clay. a) V_P (solid) and V_S (dashed) increase about 30% from the softest clay to stiffest clay; b) V_P/V_S ratio decreases about 2.2% from the softest clay to stiffest clay.

Table 1. Moduli and densities of the solids and pore used in the modeling.

	Density (g/cm^3)	Bulk Modulus (GPa)	Shear Modulus (GPa)
Brine	1.09	2.8	N/A
Gas	0.16	0.07	N/A
Quartz	2.65	36.6	45
Clay[4, 5]	2.58	21	7
Calcite	2.71	69	33
Kerogen[1,2,3]	1.45	2.9	2.7
Pyrite	4.93	147.4	132.5

[1] Blangy (1992); [2] Carmichael (1989); [3] Eastwood and Hammes (2011); [4] Han et al. (1986); [5] Tosaya (1982)

Due to its undefined structure and mineralogy, kerogen also has large uncertainties for its moduli and density. Based on vitrinite reflectance, a measurement of the maturity of the organic material, Eastwood and Hammes (2011) obtained the kerogen density as 1.45 g/cm^3 for the Haynesville Shale. The bulk and shear moduli (2.9 GPa and 2.7 Gpa) of kerogen we used were from Carmichael (1989) and Blangy (1992) (Table 1).

As for the fluid, we used Brie's fluid mixing equation (Equation 7, Brie et al., 1995) to calculate the effective fluid moduli of a brine and gas mixture. In the equation, the effective bulk modulus depends on the bulk moduli of brine (K_b) and gas (K_g), the gas saturation (S_g) and an empirical exponent (e). Bulk moduli of brine and gas are in Table 1, and the gas saturation is from the average water saturation (~25%) in the Haynesville Shale. The empirical exponent e varies from 1 for patchy saturation to 3.4 for uniformly saturation. Here the patchy saturation

provides the upper bound of effective bulk modulus of the mixed fluids, and uniform saturation provides lower bound of effective bulk modulus of the mixed fluids.

$$K_{fluid} = (K_b - K_g)(1 - S_g)^e + K_g \tag{7}$$

In Brie's fluid mixing equation, different exponents correspond to different fluid properties. We investigated how different exponents in the equation affect the model results (Figure 7). Two cases are shown. One is uniform saturation with e=3.4 (Figure 7a), and another one is very close to patchy saturation with e=1.17 (Figure 7b). In the crossplot of V_S versus V_P, the gray dots are log data from well B, and the background shows the modeling result colored by prior total porosity. The positions and colors that the data points fall into provide the porosity estimation. The models with different exponent values have different shape and color patterns, indicating they provide slightly different porosity estimations. In Figure 7a, the data points are mostly in the dark blue area, suggesting that porosity estimations are mostly close to 0; in Figure 7b, the data points are mostly in the blue and cyran areas, suggesting that porosity estimations are mostly around 5%, which is about the average porosity value of the Haynesville Shale. Therefore, for the Haynesville Shale, 1.17 is a suitable value to be used for the exponent e in Brie's fluid mixing equation.

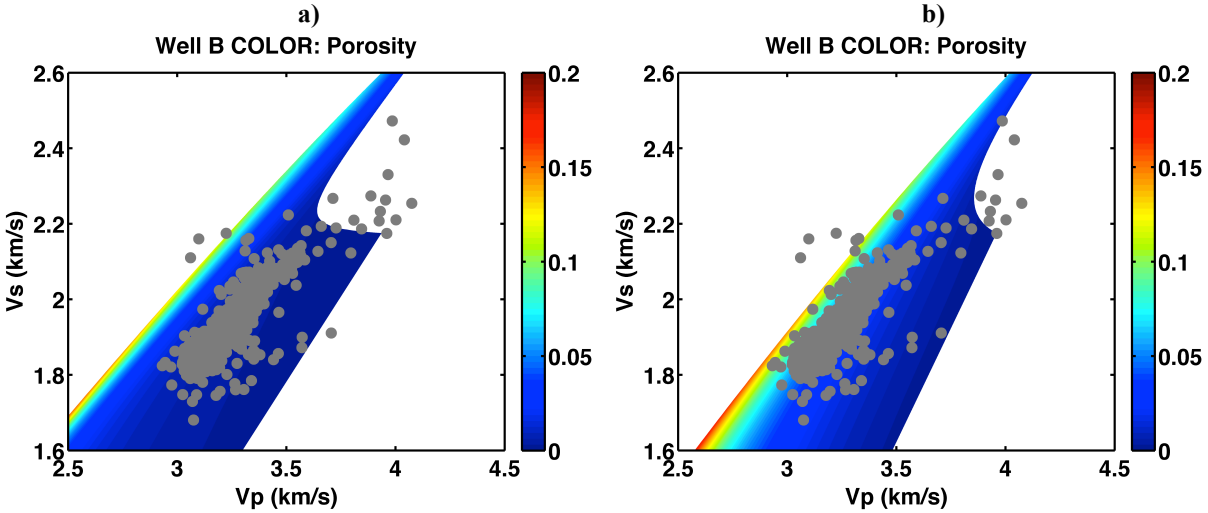

Figure 7. The effect of fluid mixing using different exponent values in Brie's fluid mixing equation (Equation 7). a) Exponent value e=3.4. In the crossplot of V_S versus V_P, gray dots are data from Well B, and background color shows the modeling result colored by prior total porosity. b) Exponent value e=1.17. Gray dots are data from Well B, and background color shows the modeling result colored by prior porosity. In this case, the data points correspond to a more accurate porosity range than in a) based on porosity from the well.

RESULTS

The modeling results are shown in Figure 8. The crossplots of V_P versus porosity (Figure 8a) and V_S versus porosity (Figure 8b) colored by prior composition demonstrate how V_P and V_S vary with prior porosity and prior composition. In both plots, gray points are observed data from Well B. When the composition varies from clay- and kerogen-rich (cold colors) to quartz- and calcite-rich (hot colors), V_P and V_S increases because the bulk moduli of quartz and calcite are larger than those of clay and kerogen. These two figures show that both V_P and V_S are modeled accurately by the combination of self-consistent model and Chapman's model. To determine if the model works for both V_P and V_S simultaneously, we generated a crossplot of V_S versus V_P, with modeling results colored by both prior distributions of porosity (Figure 7b) and composition (Figure 8c). In both figures, the variations of modeled V_P and V_S depend on the combined effects of porosity, composition and aspect ratio. Although it appears that V_S increases with porosity (Figure 7b), it is actually the increase of rock stiffness (Figure 8c) that causes the increase of V_S. Both figures (Figure 7b and 8c) show that most of the data points fall within the model, and the model followed the trends of data very well. This suggests that Chapman's model worked well for both V_P and V_S simultaneously, given the prior distributions of porosity, composition, and pore aspect ratio. Therefore, by combining modeled V_P and V_S results, we were able to estimate porosity, composition and pore aspect ratio distributions simultaneously.

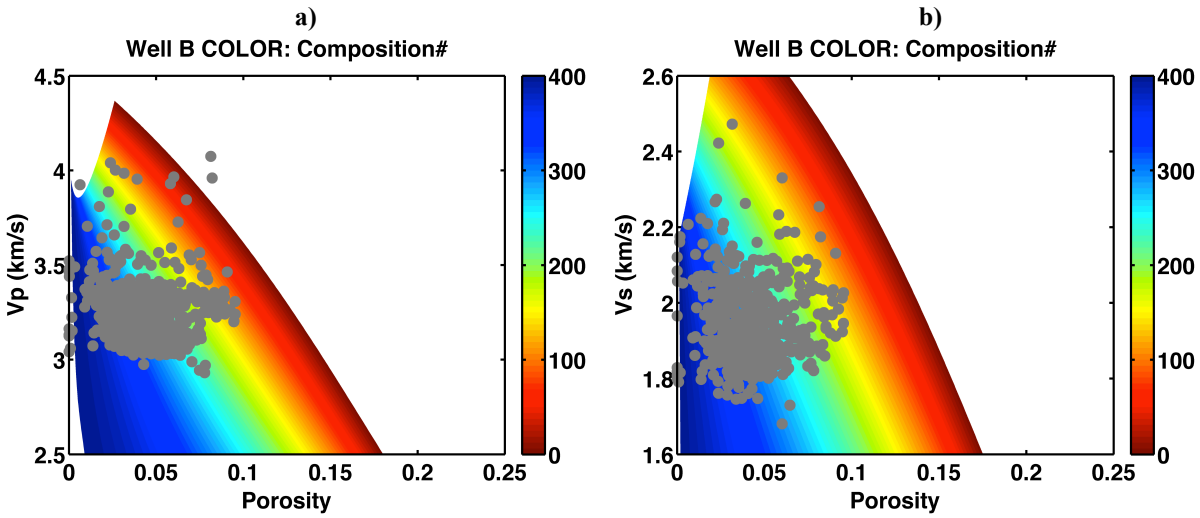

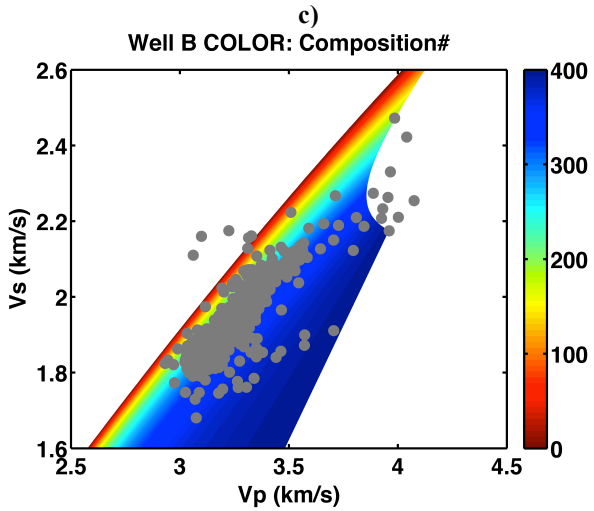

Figure 8. a) Crossplot of V_P versus porosity. Gray points are data from Well B. Background color shows the modeling result with the prior composition distribution. b) Crossplot of V_S versus porosity. Gray points are data from Well B. Background color shows the modeling result with the prior composition distribution. c) Crossplot of V_S versus V_P, colored by prior composition distribution. Almost all the data points were covered by the modeling results, and the modeling results followed the data trend very well. The data points that were missed by the model likely correspond to dolomite-rich composition excluded from the prior composition distribution.

In the model (Figure 7b and 8c), the area that covers the majority of the data points has different colors, indicating there are variations in porosity, composition and aspect ratio. Meanwhile, although a few points fall in the blue area, they correspond to a small range of porosity and composition, and relatively large uncertainty of their estimations. There are also a few points that the model missed. One possible reason is that the prior distribution of composition did not account for some extreme cases with very high dolomite percentages. Using a different parameterization of the rock physics model based on rock-type classification might make the model work even better.

Grid searching was used to estimate distributions of porosity, composition, and pore aspect ratio after rock physics modeling. The combination of the self-consistent model and Chapman's model provided trends of V_P and V_S that explain the variations in the log data. By comparing modeled V_P and V_S with observed V_P and V_S, we simultaneously inverted porosity, composition, and aspect ratio. The criteria was to accept modeled V_P and V_S that have differences less than 0.08 km/s (~2% error for V_P and ~4% error for V_S) comparing to the observed V_P and V_S. At each depth, multiple porosities, compositions and aspect ratios satisfy the criteria. We calculated the probability of each accepted value based on the number of accepted values and number of total values. In this way, we obtained not only just the best-fit reservoir properties, but also multiple fitted sets of reservoir properties with different probabilities.

The porosity estimation is shown in Figure 9. In Figure 9a, the background color shows the probability of the estimates, with the hot colors representing higher probability and cold colors representing lower probability. The black curve shows the porosity estimation with the highest probability, and the white curve is the density porosity from the log data. The porosity estimation fits the density porosity in terms of both value and the overall depth trend even though the inversion was performed independently at each depth location. The average estimated porosity is 4.6%, and density porosity is about 4.2%. They both have standard deviation of about 0.02. The histograms of density porosity (Figure 9b, top) and the best fit porosity (Figure 9b, bottom) are very similar.

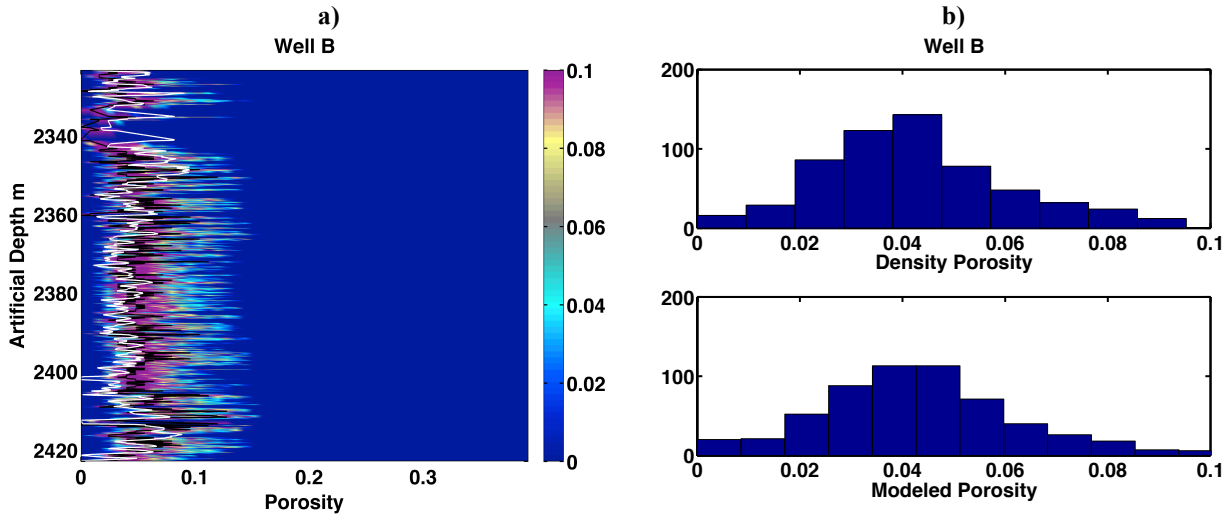

Figure 9. a) Porosity estimation. Background color represents probability, with the hot colors representing estimations with higher probability, and cold colors representing estimations with lower probability. The black curve marks the estimation with the highest probability, and the white curve shows the density porosity from log data. b) Histograms of observed and modeled porosity. Average estimated porosity is 4.6%, average density porosity is 4.2%, and both have standard deviation of about 0.02.

The composition estimate is shown in Figure 10. The best-fit composition assemblage as a function of depth in the Haynesville Shale formation is shown in Figure 10a. The average percentages for quartz, calcite, pyrite, kerogen, and clay are shown in Table 2. These percentages are very close to the ones from XRD results in Well A (Table 2). They are not exactly the same because lithology from Well A and Well B may be slightly different. Certain depths, such as 2360 m, 2406 m and 2413 m, display much higher percentages of quartz (~39%) and calcite (~31%), and much lower percentage of clay (~24%) than average within the Haynesville Shale. These features are consistent with the peaks in V_P and V_S logs (Figure 10b), and they likely correspond to more brittle zones.

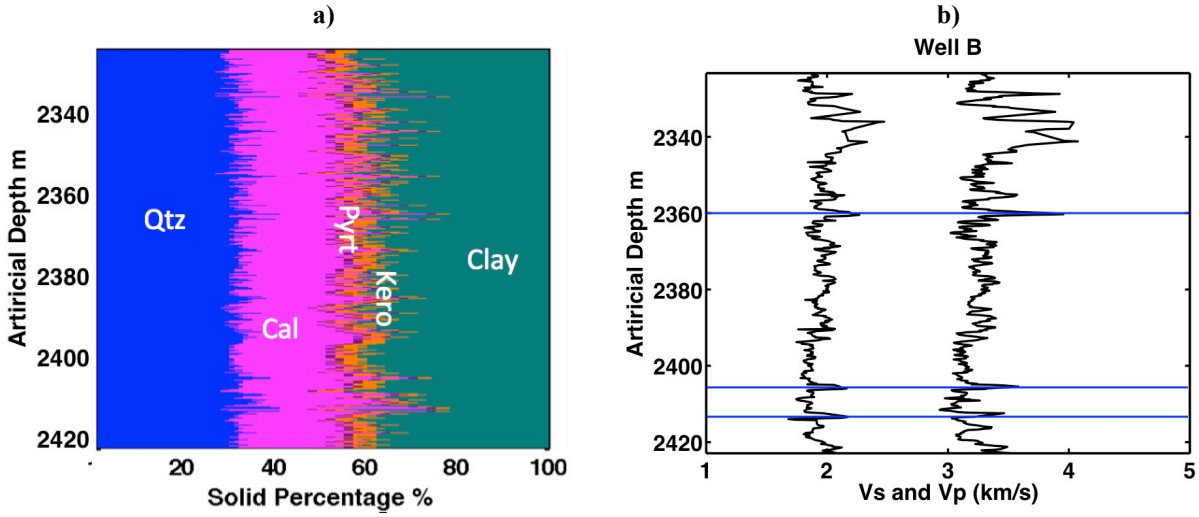

Figure 10. a) Composition assemblages along artificial depth. Each depth contains different percentages of quartz, calcite, pyrite, kerogen and clay. b) P- and S-wave velocities within the Haynesville Shale. A few peaks (marked by the blue line) of V_P and V_S at certain depths (~2360 m, ~2406 m, and ~2413 m) correspond to more brittle zones with high quartz percentage (about 39%), high calcite percentage (about 31%) and low clay percentage (about 24%).

Table 2. Comparison of compositions in percentage from modeling and XRD.

	Quartz (%)	Calcite (%)	Pyrite (%)	Kerogen (%)	Clay (%)
From Model (Well B)	31.3	23.3	2	4.7	38.7
From XRD (Well A)	31.6	25.8	2	5.3	35.4

Figure 11 shows the pore aspect ratio estimate. In Figure 11a, the background color shows the probability, with hot colors representing higher probability and cold colors representing lower probability. The black curve marks the estimation with the highest probability. Figure 11b shows the histogram of the best aspect ratio estimation, which generally follows a normal distribution. The average value of the best estimated pore aspect ratio is about 0.04, with standard deviation of about 0.016. It is difficult to verify the pore aspect ratio estimation because there is no direct measurement of pore aspect ratio. However, by looking at microstructure images of core samples, we can obtain some idea of the pore/crack/fracture shapes and partially verify the aspect ratio estimation.

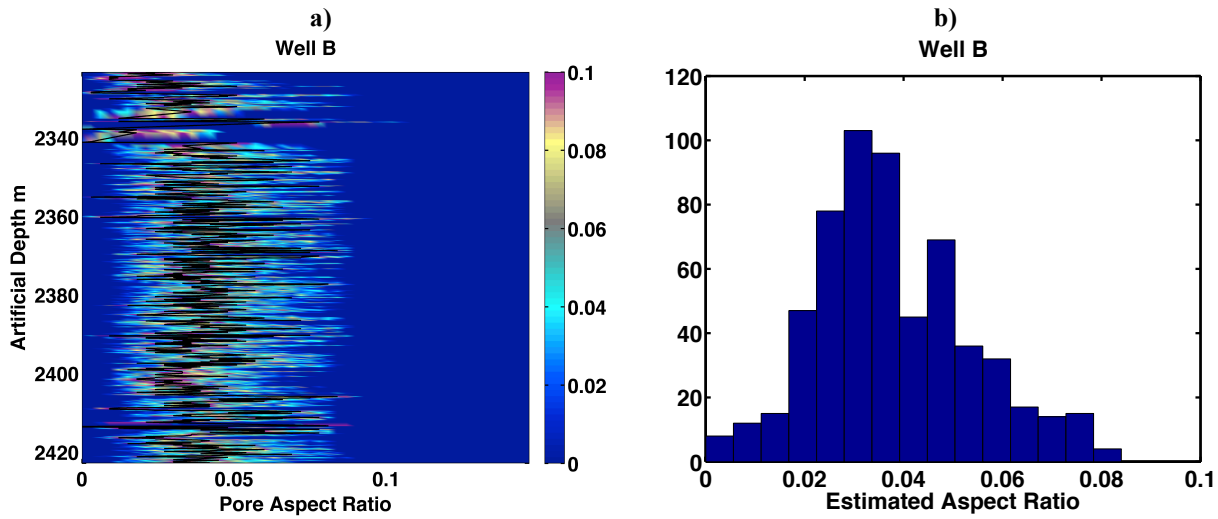

Figure 11. a) Pore aspect ratio estimation. Hot colors represent estimates with higher probability, and cold colors are for lower probability. The black curve marks the estimation with the highest probability. b) Histogram of the estimated aspect ratio. It generally follows a normal distribution, with a mean of about 0.04 and standard deviation of about 0.016.

The correlations among the estimated porosity, composition and aspect ratio are shown in Figure 12. These estimated properties are correlated in the same way as their prior distributions were correlated. As the clay percentage in estimated composition increases (composition # increases) and estimated porosity decreases (hot color to cold color), the estimated aspect ratio decreases. As clay percentage decreases (composition # decreases) and estimated porosity increases (cold color to hot color), the estimated aspect ratio increases. This is consistent with the fact that it is easier to compress soft clay than other stiffer minerals and therefore generate more flatten pores. Also, in the figure, the points with higher estimated clay percentages, lower estimated porosities and lower estimated aspect ratios are not as scattered as the ones with lower estimated clay percentages, higher estimated porosities and larger estimated aspect ratios. This means that uncertainties are relatively small for the locations with higher clay percentage, lower porosities and smaller aspect ratios.

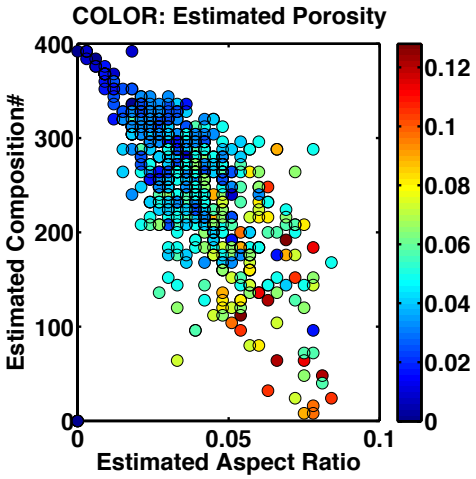

Figure 12. Correlations among estimated porosity, composition and aspect ratio. These correlations are preserved from correlations among their prior distributions. As estimated clay percentage increases and estimated porosity decreases, the estimated aspect ratio decreases. The pattern of the scattered points indicates estimation uncertainties. The more scattered points correspond to lower estimated clay percentages, higher estimated porosities, and larger estimated aspect ratios. The more condensed points correspond to higher estimated clay percentages, lower estimated porosities, and smaller estimated aspect ratios.

DISCUSSION

In this study, we placed the fluid directly into the void spaces instead of using Gassmann's fluid substitution to calculate bulk and shear moduli of the fluid-saturated rock from the dry rock frame. Gassmann's fluid substitution equations are based on several assumptions (Gassmann, 1951; Smith et al., 2003), including a homogeneous and isotropic rock matrix and low frequency so that the pore pressures are equilibrated throughout the pore space. The Haynesville Shale has extremely low permeability, and, therefore, the fluid mobility is very low. This suggests that the Haynesville Shale falls in the high-frequency regime, and the low-frequency assumption of Gassmann's equation fails (Batzle et al., 2006). In addition, our inputs into Chapman's model at about 10 kHz shows a small amount of dispersion, which also suggests that the velocity corresponds to high frequency behavior in which Gassmann's equation is not valid. Therefore, we believe it is correct to directly place the fluid in the void space during the modeling.

Reservoir properties (composition, porosity and pore shape) were estimated for the Haynesville Shale, along with the associated uncertainty. In addition to elastic properties of clay, kerogen, and fluid, there are also uncertainties in the log measurements or log calculations, such as porosity log calculation. Porosity cannot be directly measured at the log scale, so it is calculated from either the density log or neutron log. In this study, the porosity log was calculated from the density log. This calculation relied on the accuracy of density log measurement, which is very sensitive to the borehole environment. The calculation also relied on

the assumptions of fluid density and rock matrix density at each depth, which is sensitive to the composition assemblage and water saturation at each depth. In this study, composition is partially constrained by core measurements of Well A.

This study focused on reservoir characterization at a single well location. The process can be expanded to the larger seismic scale by combining the modeling with 3D surface seismic data. Seismic inversion, calibrated properly, provides V_P and V_S for a 3D volume. Once those elastic properties at the large scale are input to our algorithm, we will be able to estimate the 3D distributions of the reservoir properties. One difficulty is the scaling issue when comparing seismic velocities from rock physics models and from seismic inversion. Log data are measured at sub-meter resolution and at frequency of tens of kHz, whereas seismic data is a time measurement with frequencies of tens of Hz. Upscaling is required from the log scale to seismic scale. The Backus (1962) average, a long wavelength effective medium approximation, can be used to help solve this issue.

CONCLUSION

In this study, we developed a workflow to characterize the reservoir properties of the unconventional gas shales, and the workflow worked successfully on the Haynesville Shale. We modeled both V_P and V_S simultaneously using a combination of the self-consistent model and Chapman's model, and inverted porosity, composition and pore aspect ratio distributions from grid searching. The self-consistent model provided a porous rock matrix that contained different mineral phases and non-spherical pores as inputs in the Chapman's model. Chapman's model outputs anisotropic stiffnesses as function of frequency, porosity, fracture density, and lithology. The modeling was successful for Well B and provides relationships between the reservoir properties (porosity, composition, and pore aspect ratio) and elastic properties (V_P and V_S). The integration of the rock physics model with grid searching provided simultaneous estimates of porosity, composition and pore aspect ratio distributions for the Haynesville Shale. Estimation of porosity helps to determine gas capacity and the estimated ultimate recovery (EUR). Estimations of composition and pore aspect ratio help to understand the stiffness and brittleness of rock formations, which might contribute to locating sweet spots and identifying zones of economic production in unconventional reservoirs. Here, sweet spots are preferable locations at which to place hydraulic fractures in rock formations that contain more brittle compositions and with relatively high porosities and large pore aspect ratios.

Three-dimensional distributions of these reservoir properties will be obtained when combined with surface seismic data, from which 3D distributions of V_P and V_S can be inverted. The procedures in this study could be applied to other gas shales other than the Haynesville

Shale in order to characterize their reservoir properties. Applications to other shales, however, must begin with determining the site-specific reservoir properties that most significantly affect the seismic properties as well as the associated uncertainty.

ACKNOWLEDGEMENTS

Acknowledgment is made to the donors of the American Chemical Society Petroleum Research Fund for support (or partial support) of this research. We thank Exploration and Development Geophysics Education and Research (EDGER) Forum at The University of Texas at Austin for supporting the research. We thank BP for providing the data, and thank Ursula Hammes at the Bureau of Economic Geology (BEG) for providing XRD results. We also thank Ranjana Ghosh for helpful discussions on Chapman's model.

APPENDIX

In Chapman's Model, the following equations (Equation A1–A5) were used to calculate the five independent stiffness tensor components. These equations are the same as Equations (51), (52), (54), (59), and (61) in Chapman (2003).

$$C_{11} = (\lambda + 2\mu) - \phi_c[\frac{L_2}{\sigma_c} + \frac{32}{15}\frac{1-\nu}{(2-\nu)\pi r}\mu - (\frac{L_2}{\sigma_c} + \kappa)G_1 - (\frac{3\kappa^2}{\sigma_c} + 3\kappa)G_2 - (\frac{\lambda\kappa}{\sigma_c} + \lambda)G_3]$$
$$-\phi_p[\frac{3}{4\mu}\frac{1-\nu}{1+\nu}(3\lambda^2 + 4\lambda\mu + \frac{36+20\nu}{7-5\nu}\mu^2) - (1 + \frac{3\kappa}{4\mu})(3\kappa D_1 + \lambda D_2)]$$
$$-\phi_f[\frac{\lambda^2}{\sigma_c} - (\frac{3\lambda\kappa}{\sigma_c} + 3\kappa)F_1 - (\frac{\lambda^2}{\sigma_c} + \lambda)F_2] \quad \text{(A1)}$$

$$C_{33} = (\lambda + 2\mu) - \phi_c[\frac{L_2}{\sigma_c} + \frac{32}{15}\frac{1-\nu}{(2-\nu)\pi r}\mu - (\frac{L_2}{\sigma_c} + \kappa)G_1 - (\frac{3\kappa^2}{\sigma_c} + 3\kappa)G_2$$
$$-(\frac{(\lambda + 2\mu)\kappa}{\sigma_c} + \lambda + 2\mu)G_3]$$
$$-\phi_p[\frac{3}{4\mu}\frac{1-\nu}{1+\nu}(3\lambda^2 + 4\lambda\mu + \frac{36+20\nu}{7-5\nu}\mu^2) - (1 + \frac{3\kappa}{4\mu})(3\kappa D_1 + (\lambda + 2\mu)D_2)] \quad \text{(A2)}$$
$$-\phi_f[\frac{(\lambda + 2\mu)^2}{\sigma_c} - (\frac{3(\lambda + 2\mu)\kappa}{\sigma_c} + 3\kappa)F_1 - (\frac{(\lambda + 2\mu)^2}{\sigma_c} + (\lambda + 2\mu)F_2]$$

$$C_{44} = \mu - \phi_c[\frac{4}{15}\frac{\mu^2}{\sigma_c}(1 - G_1) + \frac{8}{5}\frac{1-\nu}{(2-\nu)\pi r}\mu] - 15\phi_p[\frac{1-\nu}{7-5\nu}\mu - \phi_f\frac{4(1-\nu)}{(2-\nu)\pi r}\mu \quad \text{(A3)}$$

$$C_{12} = \lambda - \phi_c[\frac{L_4}{\sigma_c} - \frac{16}{15}\frac{1-\nu}{(2-\nu)\pi r}\mu - (\frac{L_4}{\sigma_c} + \kappa)G_1 - (\frac{3\kappa^2}{\sigma_c} + 3\kappa)G_2 - (\frac{\lambda\kappa}{\sigma_c} + \lambda)G_3]$$
$$-\phi_p[\frac{3}{4\mu}\frac{1-\nu}{1+\nu}(3\lambda^2 + 4\lambda\mu - \frac{4(1+5\nu)}{7-5\nu}\mu^2) - (1+\frac{3\kappa}{4\mu})(3\kappa D_1 + \lambda D_2)]$$
$$-\phi_f[\frac{\lambda^2}{\sigma_c} - (\frac{3\lambda\kappa}{\sigma_c} + 3\kappa)F_1 - (\frac{\lambda^2}{\sigma_c} + \lambda)F_2] \quad \text{(A4)}$$

$$C_{13} = \lambda - \phi_c[\frac{L_4}{\sigma_c} - \frac{16}{15}\frac{1-\nu}{(2-\nu)\pi r}\mu - (\frac{L_4}{\sigma_c} + \kappa)G_1 - (\frac{3\kappa^2}{\sigma_c} + 3\kappa)G_2 - (\lambda+\mu)(1+\frac{\kappa}{\sigma_c})G_3]$$
$$-\phi_p[\frac{3}{4\mu}\frac{1-\nu}{1+\nu}(3\lambda^2 + 4\lambda\mu + \frac{4(1+5\nu)}{7-5\nu}\mu^2) - (1+\frac{3\kappa}{4\mu})(3\kappa D_1 + (\lambda+\mu)D_2)]$$
$$-\phi_f[\frac{\lambda(\lambda+2\mu)}{\sigma_c} - 3\kappa(1+\frac{\lambda+\mu}{\sigma_c})F_1 - (\frac{\lambda(\lambda+\mu)}{\sigma_c} + \lambda + \mu)F_2] \quad \text{(A5)}$$

In Equation A1-A5, λ is Lame's constant, μ is shear modulus, v is the Poisson's ratio of the matrix material, r is the aspect ratio for cracks and fractures, σ_c and κ depend on λ and μ (Equation A6), ϕ_p is round pore porosity, ϕ_c is crack porosity, and ϕ_f is fracture porosity. The D_1 and D_2 are terms to calculate pore pressure (Equation A7); G_1, G_2, and G_3 are terms to calculate crack pressure (Equation A8); and F_1 and F_2 are terms to calculate fracture pressure (Equation A9). L_2, L_3, and L_4 are calculated from λ and μ (Equation A10).

$$\sigma_c = \frac{\pi\mu r}{2(1-\nu)}$$
$$\kappa = \lambda + \frac{2}{3}\mu \quad \text{(A6)}$$

$$D_1 = [(1-\iota)\gamma + \frac{(1-\iota)\beta}{1+i\omega\tau_f} + (\iota + \frac{\iota\beta}{1+i\omega\tau_f})(\frac{1+i\omega\gamma\tau_m}{1+i\omega\tau_m})]^{-1}$$
$$\times[\frac{\iota}{3(1+K_c)} + (1-\iota)\gamma' - \frac{i\omega\tau_m}{1+i\omega\tau_m} \times (\frac{1}{3(1+K_c)} - \gamma')(\iota + \frac{\iota\beta}{1+i\omega\tau_f})] \quad \text{(A7)}$$
$$D_2 = [(1-\iota)\gamma + \frac{(1-\iota)\beta}{1+i\omega\tau_f} + (\iota + \frac{\iota\beta}{1+i\omega\tau_f})(\frac{1+i\omega\gamma\tau_m}{1+i\omega\tau_m})]^{-1} \times (\frac{\beta}{(1+K_c)(1+i\omega\tau_f)})$$

$$G_1 = \frac{i\omega\tau_m}{(1+K_c)(1+i\omega\tau_m)}$$
$$G_2 = \frac{1+i\omega\gamma\tau_m}{1+i\omega\tau_m} D_1 - \frac{i\omega\tau_m\gamma'}{1+i\omega\tau_m} \tag{A8}$$
$$G_3 = \frac{1+i\omega\gamma\tau_m}{1+i\omega\tau_m} D_2$$

$$F_1 = \frac{1}{1+i\omega\tau_f}\left[\frac{1+i\omega\gamma\tau_m}{1+i\omega\tau_m}\iota D_1 + (1-\iota)D_1 + \frac{i\omega\tau_m}{1+i\omega\tau_m}\left(\frac{1}{3(1+K_c)} - \gamma'\right)\right]$$
$$F_2 = \frac{1}{1+i\omega\tau_f}\left[\frac{i\omega\tau_f}{1+K_c} + \iota\frac{1+i\omega\gamma\tau_m}{1+i\omega\tau_m} D_2 + (1-\iota)D_2\right] \tag{A9}$$

$$L_2 = \lambda^2 + \frac{4}{3}\lambda\mu + \frac{4}{5}\mu^2$$
$$L_3 = 4\left(\lambda^2 + \frac{4}{3}\lambda\mu + \frac{8}{15}\mu^2\right) \tag{A10}$$
$$L_4 = \lambda^2 + \frac{4}{3}\lambda\mu + \frac{4}{15}\mu^2$$

In Equation A7–A9, ω is frequency, and τ_m and τ_f are relaxation time terms for cracks and fractures that account for squirt flow, which depend on crack/fracture size, fluid viscosity, grains size, and matrix bulk and shear moduli. Equation A11 gives K_c. In addition, γ and γ' are from Equation A12, where p_v and c_v are volumes of pores and cracks, K_f is bulk modulus of fluid, ι and β are from Equation A13, where ε and ε_f are crack density and fracture density.

$$K_c = \frac{\sigma_c}{K_f} \tag{A11}$$

$$\gamma = \frac{3p_v\sigma_c(1+K_p)}{4\mu c_v(1+K_c)}$$
$$\gamma' = \gamma\frac{1-\nu}{1+\nu}\frac{1}{1+K_p} \tag{A12}$$
$$K_p = \frac{4\mu}{3K_f}$$

$$\iota = \frac{\frac{4}{3}\pi\varepsilon}{\frac{4}{3}\pi\varepsilon + \phi_p}$$
$$\beta = \frac{\frac{4}{3}\pi\varepsilon_f}{\frac{4}{3}\pi\varepsilon + \phi_p} \tag{A13}$$

The stiffness tensors C_{ij}'s calculated from Equation A1–A5 are complex numbers. The real parts provide frequency-dependent velocities, and imaginary parts give frequency-dependent attenuations.

REFERENCES

Avseth, P., J. Dvorkin, G. Mavko, and J. Rykkje, 2000, Rock physics diagnostic of North Sea sands: Link between microstructure and seismic properties: Geophysical Research Letters, **27**, 2761–2764.

Avseth, P., A. Dræge, A.-J. van Wijngaarden, T. A. Johansen, and A. Jorstad, 2008, Shale rock physics and implications for AVO analysis: A North Sea demonstration: The Leading Edge, **27**, 788–797.

Bachrach, R., 2006, Joint estimation of porosity and saturation using stochastic rock-physics modeling: Geophysics, **71**, o53–o63.

Backus, G., 1962, Long-wave elastic anisotropy produced by horizontal layering: Journal of Geophysical Research, **67**, 4427-4440.

Batzle, M., D.-H. Han, and R. Hofmann, 2006, Fluid mobility and frequency-dependent seismic velocity–Direct measurements: Geophysics, **71**, N1–N9.

Bayuk, I., M. Ammerman, and E. M. Chesnokov, 2007, Elastic moduli of anisotropic clay: Geophysics, **72**, D107–D117.

Berryman, J., 1980, Long-wavelength propagation in composite elastic media I. Spherical inclusions: Journal of the Acoustical Society of America, **68**, 1809–1819.

Blangy, J. P., 1992, Integrated seismic lighologic interpretation: the petrophycical basis: Ph.D. thesis, Stanford University.

Brie, A., F. Pampuri, A. F. Marsala, and O. Meazza, 1995, Shear sonic interpretation in gas-bearing sands: SPE *30595*, 701–710.

Carmichael, R.S., 1989, *Practical handbook of physical properties of rocks and minerals*, Boca Raton, FL: CRC Press.

Castagna, J. P., M. L. Batzle, and R. L. Eastwood, 1985, Relationships between compressional-wave and shear-wave velocities in clastic silicate rocks: Geophysics, **50**, 571–581.

Chapman, M., 2001, Modelling the wide-band laboratory response of rock samples to fluid and pressure changes: Ph.D. thesis, University of Edinburgh.

Chapman, M., S. V. Zatsepin, and S. Crampin, 2002, Derivation of a microstructural poroelastic model: Geophysical Journal International, **151**, 427–451.

Chapman, M., 2003, Frequency-dependent anisotropy due to meso-scale fractures in the presence of equant porosity: Geophysical Prospecting, **51**, 369–379.

Chapman, M., 2009, Modeling the effect of multiple sets of mesoscale fractures in porous rock on frequency-dependent anisotropy: Geophysics, **74**, D97–D103.

Ciz, Radim and S. A. Shapiro, 2009, Stress-dependent anisotropy in transversely isotropic rock: Comparison between theory and laboratory experiment on shale: Geophysics, **74**, D7–D12.

Curtis, M. E., R. J. Ambrose, C. H. Sondergeld, and C. S Rai, 2010, Structural characterization of gas shales on the micro- and nano-scales: CSUG /SPE, doi: 10.2118/137693–MS.

Delle Piane, C., D. N. Dewhurst, A. F. Siggins, and M. D. Raven, 2011, Stress-induced anisotropy in brine saturated shale: Geophysical Journal International, **184**, 897–906.

Dræge, A., M. Jakobsen, and T. A. Johansen, 2006, Rock physics modeling of shale diagenesis: Petroleum Geoscience, **12**, 49–57.

Dvorkin J., and A. Nur, 1993, Dynamic Poroelasticity: A unified model with the squirt and the Biot mechanisms: Geophysics, **58**, 524–533.

Dvorkin J., R. Nolen-Hoeksema, and A. Nur, 1994, The squirt-flow mechanism: Macroscopic description: Geophysics, **59**, 428–438.

Dvorkin J. and A. Nur, 1996, Elasticity of high-porosity sandstones: theory for two North Sea data sets: Geophysics, **61**, 1363–1370.

Eastwood, R., and U. Hammes, 2011, Log model development for the Bossier and Haynesville Shales: *SPWLA 52nd Annual Logging Symposium*, Colorado Springs, Co, USA.

Eidsvik, J., P. Avseth, H. More, T. Mukerji, and G. Mavko, 2004, Stochastic reservoir characterization using prestack seismic data: Geophysics, **69**, 978–993.

Gal, D., J. Dvorkin, and A. Nur, 1998, A physical model for porosity reduction in sandstones: Geophysics, **63**, 454–459.

Gassmann, F., 1951, Uber die elastizitat poroser medien: Veirteljahrsschrift der Naturforschenden Gesellschaft in Zurich, **96**,1-23.

Grana, D. and E. Della Rossa, 2010, Probabilistic reservoir-properties estimation integrating statistical rock physics with seismic inversion: Geophysics, **75**, o21–o37.

Hammes, U., H. S. Hamlin, and E. E. Thomas, 2011, Geologic analysis of the Upper Jurassic Haynesville Shale in east Texas and west Louisiana: AAPG Bulletin, **95**, 1643–1666.

Han, D.-H., A. Nur, and D. Morgan, 1986, Effects of porosity and clay content on wave velocities in sandstones: Geophysics, **51**, 2093–2107.

Hornby, B., L. M., Schwartz, and J. A. Hudson, 1994, Anisotropic effective–medium modeling of the elastic properties of shales: Geophysics, **59**, 1570–1583.

Horne, S., J. Walsh, and D. Miller, 2012, Elastic anisotropy in the Haynesville Shale from dipole sonic data: First Break, **30**, 37–41.

Jiang, M. and K. T. Spikes, 2012, Estimation of the porosity and pore aspect ratio of the Haynesville Shale using the self-consistent model and a grid search method: 82th Annual International Meetings, SEG, Expanded Abstracts, accepted.

Kuila, U., D. N. Dewhurst, A. F. Siggins, and M. D. Raven, 2011, Stress anisotropy and velocity anisotropy in low porosity shale: Tectonophysics, **503**, 34–44.

Kuster, G. T. and M. N. Toksoz, 1974. Velocity and attenuation of seismic waves in two-phase media: Geophysics, **39**, 587-618.

LaValle, S .M., M. S. Branicky, and S. R. Lindemann, 2004, On the relationship between classical grid search and probabilistic roadmaps: International Journal of Robotics Research, **23**, 673–692.

Mavko, G., T. Mukerji, and J. Dvorkin, 2009, *The Rock Physics Handbook: Tools for Seismic Analysis of Porous Media*. Cambridge University Press, Cambridge.

Moyano, B., K. T. Spikes, T. A. Johansen, and N. H. Mondol, 2012, Modeling compaction effects on the elastic properties of clay-water composites: Geophysics, **77**, D171–D183.

Mukerji, T., A. Jorstad, P. Avseth, G. Mavko, and J. R. Granli, 2001, Mapping lithofacies and pore-fluid probabilities in a North Sea reservoir: seismic inversions and statistical rock physics: Geophysics, **66**, 988–1001.

Nadri, D., J. Sarout, A. Bona, and D. Dewhurst, 2012, Estimation of the anisotropy parameters of transversely isotropic shales with a tilted symmetry axis: Geophysical Journal International, **190**, 1197–1203.

O'Connell, R. and B. Budiansky, 1974, Seismic velocities in dry and saturated crack solids: Journal of Geophysical Research, **79**, 5412–5426.

Pervukhina, M, B. Gurevich, P. Golodoniuc, and D. N. Dewhurst, 2011, Parameterization of elastic stress sensitivity in shales: Geophysics, **76**, WA147–WA155.

Rimstad, K., P. Avseth, and H. More, 2012, Hierarchical Bayesian lithology/fluid prediction: A North Sea case study: Geophysics, **77**, B69–B85.

Saffer, D. M. and C. Marone, 2003, Comparison of smectite- and illite-rich gouge frictional properties: application to the updip limit of the seismogenic zone along subduction megathrusts: Earth and Planetary Science Letters, **215**, 219–235.

Sen, M. and P. L. Stoffa, 1995, *Global optimization methods in geophysical inversion*, ELSEVIER Science.

Spikes, K. T., T. Mukerji, J. Dvorkin, and G. Mavko, 2007, Probabilistic seismic inversion based on rock-physics models: Geophysics, **72**, R87–R97.

Smith, T. M., C. H. Sondergeld, and C. S. Rai, 2003, Gassmann fluid substitutions: A tutorial: Geophysics, **68**, 430-440.

Theng, B. K. G., 1974, *The chemistry of clay-organic reactions*, pp. 343, Hilger, London.

Thomsen, L., 1986, Weak elastic anisotropy: Geophysics, **51**, 1954–1966.

Tosaya, C. A., 1982, Acoustical properties of clay-bearing rocks: Ph.D. thesis, Stanford University.

Tosaya, C. A. and A. Nur, 1982, Effects of diagenesis and clays on compressional velocities in rocks: Geophysical Research Letters, **9**, 5–8.

Vanorio, T., M. Prasad, and A. Nur, 2003, Elastic properties of dry clay mineral aggregates, suspensions and sandstones: Geophysical Journal International, **155**, 319–326.

Vanorio, T., T. Mukerji, and G. Mavko, 2008, Emerging methodologies to characterize the rock physics properties of organic-rich shales: The Leading Edge, **27**, 780–787.

Wang, F. P. and U. Hammes, 2010, Effects of reservoir factors on Haynesville fluid flow and production: World Oil, **231**, D3–D6.

Wang, Z., H. Wang, and M. E. Cates, 2001, Effective elastic properties of solid clays: Geophysics, **66**, 428–440.

Whitney, G., 1990, Role of water in the smetite-to-illite reaction: Clays and Clay Minerals, **38**, 343–350.